Journal of
Manufacturing and Materials Processing

MDPI

Article

Mechanical and Cellular Evaluations of ACP-Enriched Biodegradable Micromolded PLA/PCL Bone Screws

Min-Wen Wang [1,*], Wei-Young Wang [1], Chun-Ming Chen [1] and Chun-Chieh Tseng [2]

[1] Mechanical Engineering Department, National Kaohsiung University of Science and Technology, Kaohsiung City 807618, Taiwan; f110142168@nkust.edu.tw (W.-Y.W.); abc1099103133@gmail.com (C.-M.C.)
[2] Combination Medical Device Technology Division, Medical Devices R&D Service Department, Metal Industries Research & Development Centre, Kaohsiung 81160, Taiwan; cctseng0915@gmail.com
* Correspondence: mwwang@nkust.edu.tw

Abstract: Nanoscale amorphous calcium phosphate (ACP) exhibits superior bioactivity, degradability, and osteoblast adhesion compared to hydroxyapatite (HAp), making it a promising bioactive ceramic material for bone regeneration applications. This study explores the integration of ACP as a bioactive additive in polylactic acid/polycaprolactone (PLA/PCL) composites. Nanoscale ACP powder was synthesized through low-temperature wet chemical methods without additional reagents. The composite, consisting of 10 wt.% ACP, 80 wt.% PLA, and 20 wt.% PCL, achieved optimal tensile strength (>12 MPa) and elongation (>0.1%). Utilizing the Taguchi experimental design, the microinjection molding parameters were optimized, and they are a material temperature of 190 °C, an injection speed of 50 mm/s, and a holding pressure speed of 30 mm/s. Variance analysis identified the injection speed to be the most significant factor, contributing 50.73% to the overall effect. Immersing ACP in simulated body fluid (SBF) for six hours reduced its calcium ion concentration by 28%, with this concentration stabilizing thereafter. Biocompatibility was confirmed through an MTT assay with NIH-3T3 cells, demonstrating the PLA/PCL/ACP composite's compatibility. Bone differentiation and mineralization tests showed the enhanced performance of both ACP and the composite material. Degradation tests indicated an initial 0.29% weight increase in the first week, followed by a 2% reduction by the fifth week. These results underscore the PLA/PCL/ACP composite's excellent mechanical properties, biocompatibility, and suitability for injection molding, positioning it as a strong candidate for biodegradable bone screw applications.

Keywords: biodegradable bone screws; polylactic acid (PLA); polycaprolactone (PCL); amorphous calcium phosphate (ACP); micromolding; biomedical composites

check for updates

Academic Editor: Lawrence E. Murr

Received: 19 March 2025
Revised: 26 April 2025
Accepted: 1 May 2025
Published: 7 May 2025

Citation: Wang, M.-W.; Wang, W.-Y.; Chen, C.-M.; Tseng, C.-C. Mechanical and Cellular Evaluations of ACP-Enriched Biodegradable Micromolded PLA/PCL Bone Screws. *J. Manuf. Mater. Process.* **2025**, *9*, 154. https://doi.org/10.3390/jmmp9050154

Copyright: © 2025 by the authors. Licensee MDPI, Basel, Switzerland. This article is an open access article distributed under the terms and conditions of the Creative Commons Attribution (CC BY) license (https://creativecommons.org/licenses/by/4.0/).

1. Introduction

Accidental and sports-related injuries often result in bone fractures and ligament damage that require immediate stabilization to promote proper healing and reconstruction [1]. Traditionally, bone screws manufactured from metals—such as titanium alloys, pure titanium, stainless steel, and cobalt–chromium alloys—have been employed to achieve this stabilization [2,3]. Despite their excellent mechanical strength, these metallic implants exhibit significant clinical drawbacks. For instance, the wear of the oxidation layer can lead to metal ion release, inciting tissue inflammation and sometimes necessitating secondary removal surgeries, which not only cause patient discomfort but also waste medical resources [4]. In addition, the high Young's modulus of metals can result in stress shielding

and subsequent bone resorption, a particularly serious problem in pediatric patients where impaired load distribution may affect future bone growth [5].

To overcome these limitations, the move toward biodegradable alternatives has gained momentum. Magnesium, an essential element with high biocompatibility and degradability, has been investigated as an implant material because its Young's modulus (40–45 GPa) is closer to that of human bone (5–17 GPa) [6,7]. However, when used in biodegradable alloys, magnesium tends to degrade too rapidly in vivo, undermining its long-term stability as an implant [8].

Polymeric materials such as polylactic acid (PLA) have also been introduced in the manufacture of bone screws. Several companies—including Taiwan's Union Biomedical and the U.S.-based Arthrex and Biosteon—have developed PLA-based screws that boast good biocompatibility and sufficient mechanical strength for ligament repair [9]. Nevertheless, PLA presents its own set of clinical challenges. Reports have identified issues with PLA implants, including disintegration, osteolysis, chondrolysis, cyst formation, and allergic reactions [9]. Moreover, the inherent brittleness of PLA makes it susceptible to rupture after implantation, potentially leading to the inadequate healing of ligament injuries if timely intervention is not pursued [10,11].

To address PLA's brittleness, polycaprolactone (PCL)—a ductile polymer—can be blended with PLA to improve the overall ductility and reduce the risk of cracking. Research by Hassanajili et al. [12] suggests that PLA/PCL composites not only enhance mechanical performance but also benefit from the incorporation of biomedical ceramics that promote bone cell proliferation and attachment, thereby enhancing integration with host bone.

Calcium phosphates (CaPs) have long been used as bioactive ceramics for bone repair and regeneration. In particular, hydroxyapatite (HAp) closely mimics the inorganic phase of bone due to its similar structure and composition [13,14]. However, conventional crystalline HAp often experiences excessive grain growth during high-temperature processing, which diminishes its biological activity. In contrast, amorphous calcium phosphate (ACP)—synthesized via low-temperature wet chemical methods—produces microscale-to-nanoscale particles with higher solubility, leading to improved bioactivity, biodegradability, and osteoblast adhesion [15].

Advances in micromolding technology further contribute to this field by enabling the fabrication of intricately designed, high-precision biodegradable bone screws that meet rigorous clinical demands [16]. Integrating nanoscale ACP into PLA/PCL composites via these precise molding techniques represents a cutting-edge strategy for optimizing both mechanical performance and osseointegration [17]. Recent investigations have also provided valuable insights into PLA's biodegradation behavior [18], the microstructure-based magneto-mechanical modeling of composite systems [19], and composite formulation strategies extrapolated from studies on supplementary cementitious materials [20]. Furthermore, incorporating ACP into biodegradable polymer matrices has been shown to enhance osteogenic differentiation and bone regeneration capabilities [21].

Collectively, these studies underscore the critical importance of biocompatibility, mechanical integrity, and controlled degradation in the development of advanced biomaterials for orthopedic applications. Building on this foundation, this study aims to develop biodegradable bone screws composed of a PLA/PCL blend reinforced with ACP. Utilizing low-temperature wet chemical synthesis to produce bioactive ACP and employing injection molding technology, this study endeavors to create a novel, safe, effective, and cost-efficient bone screw implant. The ultimate goal of this study is to enhance the treatment of bone fractures and ligament injuries while reducing patient discomfort and minimizing the need for secondary interventions.

2. Materials and Methods

2.1. Synthesis of Nanoscale Amorphous Calcium Phosphate

Somrania et al. [22] proposed a low-temperature wet synthesis method for amorphous calcium phosphate (ACP). To begin, a 0.36 M nitrate solution and a 0.16 M phosphate solution were prepared, each containing 40 mL of 28 wt.% ammonium hydroxide (NH_4OH). The nitrate solution was added to the phosphate solution, resulting in the rapid precipitation of ACP. This mixture was then immediately poured into 3 L of deionized water (containing 15 mL of 28 wt.% NH_4OH) to inhibit further crystallization. After washing, the solution was divided into bottles and centrifuged to separate the powder from the solution based on density differences. The excess water was decanted, and the ACP was extracted and frozen at −18 °C to prevent crystallization during storage. The frozen ACP was then freeze-dried at −40 °C and 1.3 Pa to sublimate the ice crystals, resulting in the ACP powder. The ACP powder is shown in Figure 1.



Figure 1. ACP powder.

2.2. Preparation of Composite Material

A mixture of 80 wt.% PLA and 20 wt.% PCL exhibited superior mechanical properties [23,24]; thus, this ratio was used as the polymer composite base in this study. The ACP powder was added in amounts ranging from 5 wt.% to 30 wt.% for experimental testing. PLA (Corbion Purac Group, Luminy@L175)/PCL (Perstorp, Skåne, Sweden, Capa 6800)/ACP composites were mixed using a Brabender mixer (Plasti-Corder Lab-Station, Duisburg, Germany) at 190 °C and 50 rpm for 10 min. Torque and temperature curves were recorded to determine the uniformity of the material mixing, as shown in Figure 2. Cross-sectional analysis was conducted on the blended materials and injection-molded bone screws to evaluate the uniformity.

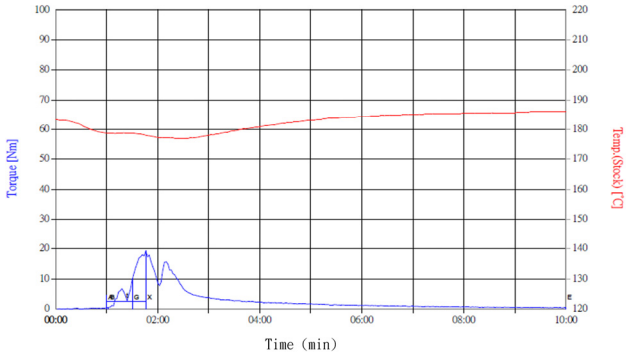


Figure 2. Real-time temperature and torque profiles during mixing of PLA/PCL/ACP.

2.3. Material Characterization

This study used a scanning electron microscope (SEM) to observe the surface characteristics of the ACP powder. To enhance conductivity, the non-conductive synthesized powder

was coated with gold using a vacuum sputter coater at 20 mA for 60 s. Energy-dispersive X-ray spectroscopy (EDX) was then employed to analyze its elemental composition. X-ray diffraction (XRD) was used to analyze the crystal structure, chemical composition, and physical properties of the synthesized material. To confirm the material was ACP, XRD was conducted with a 2θ angle range of 10° to 100°, operating at 30 kV and 20 mA.

2.4. Specimen Molding for Tensile Test

For this test, tensile specimens were prepared according to the ASTM-D638 [25]. The specimens measured 63.5 mm in length, 9.53 mm in width, and 3.2 mm in thickness [25]. A compression molding machine (Ling Fong 30 Ton Hot Press, Tainan, Taiwan) was used for specimen preparation. The material mixed by the Brabender mixer was cut into appropriate sizes, placed in the mold cavity, melted at a mold temperature of 200 °C, and compressed at a pressure of 25 kg/cm^2 for 10 min. Afterward, the mold temperature was cooled to 60 °C using a water circulation system.

2.5. Injection Molding Experiment

The bone screw design is shown in Figure 3. This study utilized a Battenfeld Microsystem 50 micromolding machine for injection molding and employed the Taguchi experimental method to determine the optimal injection molding parameters and their effect on the shrinkage of bone screw injection molding. The control factors selected for the experiment were the melt temperature, injection speed, and holding speed. Before the experiment, Moldex3D analysis was used to determine the fixed parameter values. During actual injection, the processing window was established, the control factor level values were set, and the Taguchi experiment was conducted. The shrinkage rate of the molded bone screw size served as the quality indicator. A smaller shrinkage rate indicated better quality; thus, the experiments were conducted with the objective of achieving the smallest possible shrinkage.

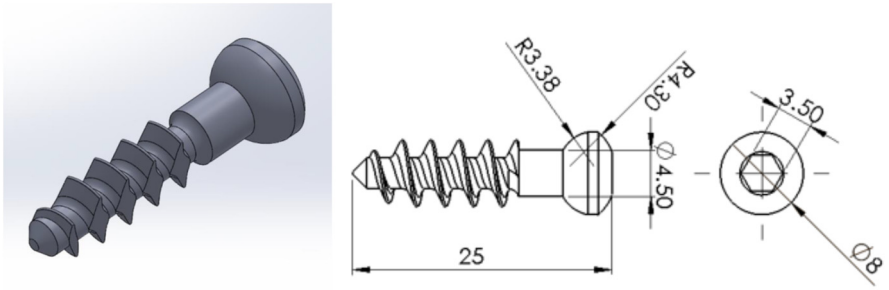


Figure 3. Design of bone screw.

2.5.1. Mold Filling Speed Parameter Setting

From a fluid mechanics perspective, the faster a fluid flows, the greater the resistance it must overcome, resulting in higher pressure requirements. Polymers are non-Newtonian fluids with a shear-thinning effect; as speed increases, shear rate increases and viscosity decreases. Therefore, the injection pressure does not necessarily increase with higher injection speeds. This study utilized different injection speeds to analyze the mold filling flow. As shown in Figure 4, at an injection speed of 60 mm/s, the required injection pressure was lower. Consequently, 60 mm/s was selected as the starting parameter value for experiments with actual injection molding.

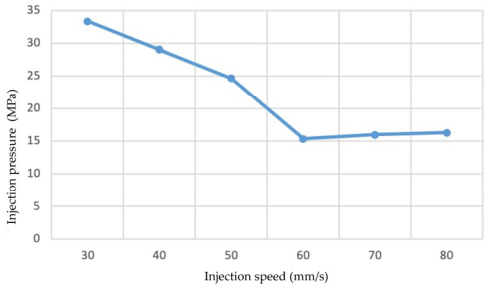
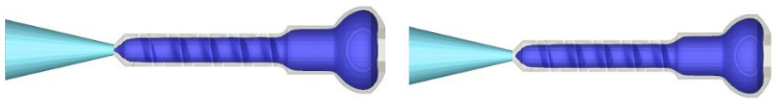


Figure 4. Relationship between injection speed and injection pressure.

2.5.2. Holding Time Parameter Setting

One criterion for setting the holding time is to adjust it according to the solidification time of the melt at the gate. If pressure holding stops before the melt solidifies, the holding effect is poor and the product shrinks. Conversely, if pressure is maintained after the melt solidifies, it can lead to excessive pressure holding and residual stress. Moldex3D was used to simulate the holding process under conditions of 60 mm/s injection speed, 190 °C melt temperature, and 30 °C mold temperature. As shown in Figure 5, the gate had not solidified at 2.965 s of packing but had solidified at 3.146 s of holding. Therefore, 4 s was selected as the holding time in the subsequent Taguchi experiment.



(**a**) (**b**)

Figure 5. Melt state at gate: (**a**) holding time: 2.965 s; (**b**) holding time: 3.146 s.

2.5.3. Cooling Parameter Settings

The typical mold temperature setting for molding PLA is 20–30 °C [26] to ensure sufficient cooling. To avoid warping caused by uneven shrinkage after ejection, it is recommended to cool to a temperature difference of less than 10 °C in the part before ejection [27]. From the mold flow analysis results in Figure 6, it is evident that, with a cooling time of 35 s, the maximum temperature difference in the mold cavity is 6.1 °C. Therefore, the cooling time for the subsequent molding experiment is set to 35 s.

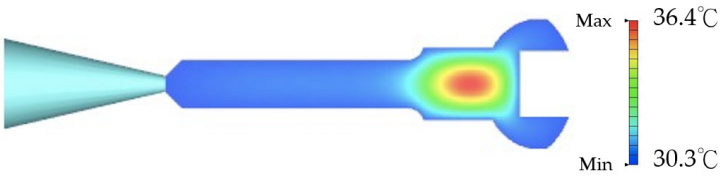
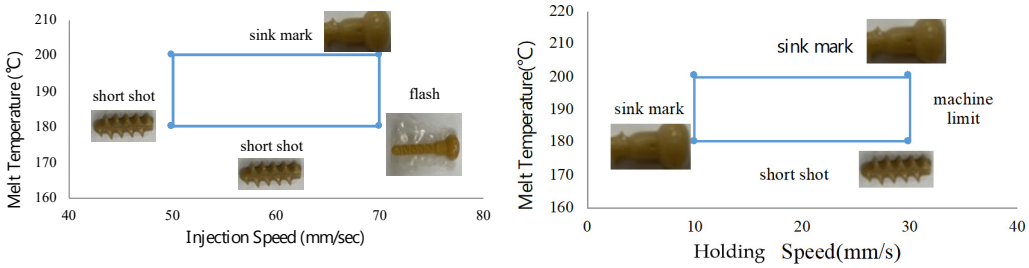


Figure 6. Temperature distribution at a cooling time of 35 s.

2.5.4. Processing Window

Before planning the Taguchi experiment, this study first identified the processing windows of the control factors through trial molding, as shown in Figure 7. For the PLA used in this study, a melting temperature of 180–220 °C is recommended [26]. In the molding test, when the material temperature is below 180 °C, short shots occur due to premature cooling. Conversely, temperatures above 200 °C result in defects such as sink marks and burrs. The injection pressure–injection speed analysis in Figure 4 indicates that an injection speed of 60 mm/s has a relatively low injection pressure. Therefore, the injection speed processing window experiment started from 60 mm/s. At speeds

lower than 50 mm/s, short shots occur, whereas speeds exceeding 70 mm/s result in flash formation on the bone screw. The pressure-holding process of the Microsystem 50 micro injection machine is controlled by the plunger speed rather than pressure, unlike general injection machines. When the holding speed is below 15 mm/s, effective holding cannot be achieved, leading to sink marks on the bone screw surface. However, well-molded bone screws were obtained at all settings from 15 mm/s to the machine's maximum hold speed of 33 mm/s.



(**a**) (**b**)

Figure 7. Processing window: (**a**) melt temperature vs. injection speed; (**b**) melt temperature vs. holding speed.

2.5.5. Parameter Settings for Bone Screw Molding Process

The processing window experiment results suggest that the range of the three Taguchi experimental control factors are as follows: a material temperature between 180 and 200 °C, an injection speed between 50 and 60 mm/s, and a holding speed between 10 and 33 mm/s. Each factor has three levels within this processing range, with the highest holding speed set at 30 mm/s. Table 1 shows the level values of each factor.

Table 1. Control factor levels.

Level/Factor	Melt Temperature (°C)	Injection Speed (mm/s)	Holding Speed (mm/s)
1	180	50	10
2	190	60	20
3	200	70	30

The mold flow analysis results in Figures 5 and 6 suggest that a holding time of 4 s, a cooling time of 35 s, and a back pressure of 15 bar can avoid bubbles in the finished product. During the Taguchi experiment, the metering amount and the plasticizing screw speed were kept constant, and Table 2 presents the values of these parameters. Since each of the three control factors has three levels in this experiment, the L9 orthogonal table was used for the Taguchi experiment, as shown in Table 3.

Table 2. Fixed parameters in experiment.

Fixed Parameter	Value
Holding time	4 s
Cooling time	35 s
Back pressure	15 bar
Screw speed	80 rpm
Metering volume	720 mm^3

Table 3. L9 orthogonal array.

Group	Melt Temperature (°C)	Injection Speed (mm/s)	Holding Speed (mm/s)
1	180	50	10
2	180	60	20
3	180	70	30
4	190	50	20
5	190	60	30
6	190	70	10
7	200	50	30
8	200	60	10
9	200	70	20

2.5.6. Taguchi Experiment

To ensure the optimal bone screw injection molding quality, a 30 min preheating step was performed before the injection molding experiments to stabilize the molding environment. Five bone screws were sampled for each set of molding parameters, with their lengths and outer diameters measured as illustrated in Figure 8. The mold used for producing the bone screws has a length of 25.009 mm and a head diameter of 8.004 mm. The dimensions of the molded bone screws were compared to those of the mold to calculate the length and radial shrinkage rates using Equation (1). Based on the shrinkage rate, the S/N ratio for each Taguchi group was calculated using Equation (2).

$$\text{Shrinkage Rate (\%)} = (\text{Mold Size} - \text{Product Size})/\text{Mold Size} \times 100\% \quad (1)$$

$$S/N_{STB} = -10log\left(\frac{1}{n}\sum_{i=1}^{n} y_i^2\right) \quad (2)$$

where y_i is the quality characteristic of the i-th sample, and n is the number of samples.

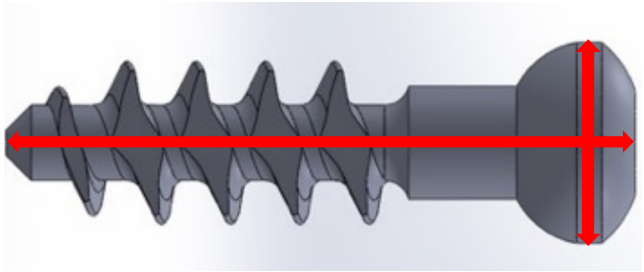


Figure 8. Schematic diagram of bone screw measurement positions.

2.5.7. Analysis of Bone Screw Internal Structure

To evaluate the uniformity of ACP powder distribution after injection molding, cross-sectional studies were conducted on the molded bone screws. The bone screws were embedded in BUEHLER cold mounting resin (SamplKwick 20-3560) and prepared for metallographic analysis. Sandpaper with grit sizes ranging from P120 to P4000 was used for grinding, followed by surface polishing. Due to the non-conductive nature of polymer bone screws, gold sputtering was performed on the polished surfaces to facilitate the subsequent SEM analysis.

2.6. Water Hardness Test for Calcium Ion Release

This study used water hardness testing to measure calcium ion (Ca^+) release concentrations from ACP and HAp immersed in simulated body fluid (SBF). ACP and HAp were immersed in an SBF buffer solution containing an indicator that turned wine red. The

ethylenediaminetetraacetic acid (EDTA) disodium salt solution was titrated into the sample solution using a burette. When all Ca^+ ions were chelated, the solution color changed from red to blue, indicating the titration endpoint.

To prepare the standard calcium solution, 0.1 g of anhydrous calcium carbonate was dissolved in 1 M hydrochloric acid, followed by the addition of 100 mL of ultrapure water to achieve a 1 mg/mL (1000 ppm) concentration. The EDTA titration solution was prepared by dissolving 0.14612 g of EDTA in 500 mL of ultrapure water to obtain a 0.001 M solution.

The calcium content of the EDTA solution was determined using Equation (3):

$$\text{Moles of Ca in EDTA Solution}\left(\frac{\text{mg}}{\text{ml}}\right) = \frac{Calcium\ content\ of\ standard\ solution\ (mg)}{Volume\ of\ EDTA\ titration\ (ml)} \quad (3)$$

The calcium concentration of ACP and HAp solutions was calculated based on the volume of EDTA titrated, as shown in Equation (4):

$$Ca^+ \text{ Concentration} = \text{Moles of Ca in EDTA Solution } \times \text{Titration Volume} \quad (4)$$

2.7. Biocompatibility, Bone Differentiation, and Bone Mineralization Ability Tests

Following the ISO 10993-5 [28], materials were immersed in bone cell culture media (low-glucose DMEM supplemented with 100 μg/mL ascorbic acid, 10 μg/mL non-essential amino acids (L-Glutamine), 100 μg/mL penicillin/streptomycin, 10% fetal bovine serum (FBS), and 0.01% vitamin C) at 37 °C for 72 h in a shaking water bath to collect the extract solution. NIH/3T3 fibroblast cells (mouse fibroblast cell line) and mouse bone marrow cells (D1 cell line) were used for testing.

Biocompatibility Test (MTT Assay): Each well of a sterile 96-well plate was seeded with 1×10^4 cells in 100 μL of culture medium. After adding 100 μL of the extract solution, the plate was incubated at 37 °C and 5% CO_2 for 24 h. Following incubation, 100 μL of MTT solution was added to each well, and the plate was incubated for an additional 2 h. MTT reacted with mitochondrial enzymes of live cells, producing purple-blue formazan crystals, which were then dissolved in DMSO to form a purple solution. The absorbance of this solution was measured at 570 nm using an ELISA reader, with higher absorbance values indicating better biocompatibility.

Bone Differentiation Ability Test (ALP Assay): A 48-well plate was prepared with 2×10^4 cells in 200 μL of culture medium. After 24 h, the supernatant was removed and replaced with the extract solution. Following a further 24 h of cell culture, osteoinduction medium (OIM) was introduced to promote cell differentiation and mineralization. After 48 h of culture with OIM, 80 μL of the tissue culture fluid was transferred to a 96-well sterile plate, and 50 μL of phosphate solution was added to react at room temperature in the dark for 1 h. The alkaline phosphatase activity was measured using Biovision's ALP assay reagent, with the absorbance reading at 405 nm using an ELISA reader. Higher absorbance values indicated higher alkaline phosphatase activity, and the relative percentage of activity was calculated by setting the control group's measured value as 100%.

Bone Mineralization Ability Test: Sterile 48-well plates were prepared with 2×10^4 cells per well in 200 μL of culture media. After 24 h of incubation, the supernatant was removed and replaced with the extract solution. The extract solution and cells were incubated for 24 h, followed by the addition of osteoinduction medium (OIM) to promote bone differentiation and mineralization. After washing with phosphate-buffered saline (PBS), the cells were immersed in 10% formalin for 20 min, then washed twice with DI water and stained with Alizarin Red S (ARS) for 10 min. The cells were rinsed with purified water 2-3 times and allowed to dry. Alizarin red stains calcium deposits, forming an orange-red precipitate. Once dried, 200 μL of 10% acetic acid was added to each well, and 100 μL was

transferred to a 96-well sterile plate. The absorbance was measured at 405 nm using an ELISA reader (Thermo Fisher Scientific, Waltham, MA, USA). The absorbance value of the tissue culture medium group served as the reference value, and the calcium deposition ability was judged by the absorbance value of the test groups relative to the reference value, with higher absorbance values indicating greater calcium deposition and better bone mineralization induction ability.

2.8. Degradation Test

This test followed the ASTM F1635-11 [29] to evaluate the degradation of injection-molded bone screws. Bone screws were placed in centrifuge tubes filled with simulated body fluid (SBF) and incubated in a shaking water bath at 37 °C, with agitation set to 10 rpm. Weight and pH changes were recorded weekly for four weeks. Before weighing, the bone screws were dried in an oven at 60 °C for 2 h to remove internal moisture and minimize measurement errors. The collected data were used to plot degradation and pH curves.

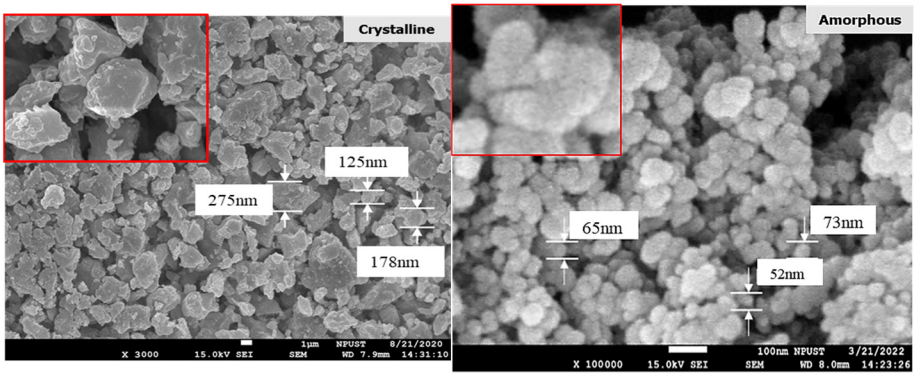
To prepare the simulated body fluid (SBF), reagents were sequentially added to 900 mL of ultrapure water using a magnetic stirrer for complete dissolution, following Oyane et al. [30]. The reagents were added in the following order and amounts (g/L): NaCl (8.035), $NaHCO_3$ (0.355), KCl (0.225), $K_2HPO_4 \cdot 3H_2O$ (0.231), $MgCl_2 \cdot 6H_2O$ (0.311), 1 M HCl (19.5), $CaCl_2$ (0.292), Na_2SO_4 (0.072), and TRIS (6.118). The solution was then adjusted to a pH of 7.40 at 36.5 °C using 1 M HCl and diluted to a final volume of 1000 mL with ultrapure water.

3. Results and Discussion

3.1. Material Measurement and Analysis

3.1.1. Scanning Electron Microscope with Energy-Dispersive Spectroscopy

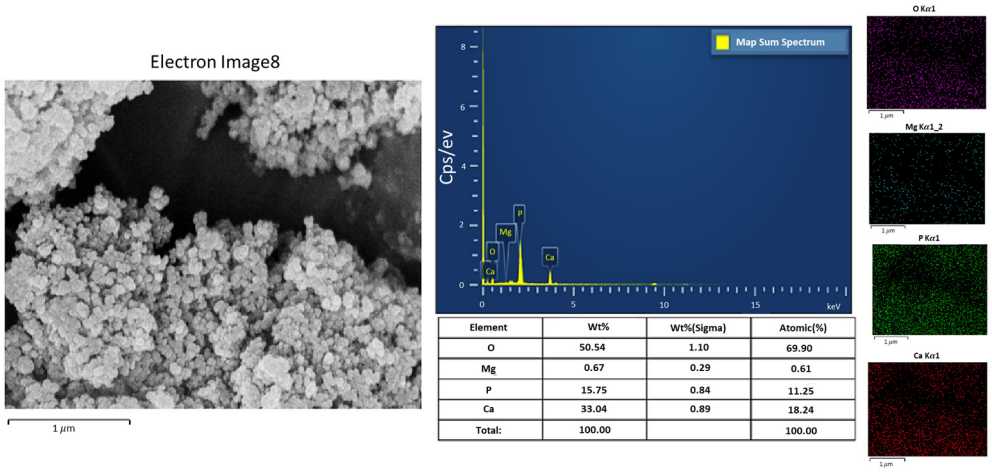
The synthesized ACP powder was analyzed using SEM. The crystalline powder, shown in Figure 9a, exhibited clear particle morphology with distinct angular shapes, and the particle size ranged from approximately 125 to 275 nm. The amorphous powder, shown in Figure 9b, displayed blurred, semi-transparent particle morphology, with particle sizes ranging from approximately 52 to 73 nm, confirming that the powder particles were at the nanoscale level. In comparison with previous studies (e.g., [21,22]), our observed particle sizes for both the crystalline and amorphous phases fall within the reported nanoscale range for ACP (typically 50–300 nm). This consistency not only validates our synthesis method but is also beneficial; the uniform and relatively smaller particle size of the amorphous phase is advantageous for enhancing surface reactivity and dissolution rates—key factors that can promote faster ion release, bone cell proliferation, and mineralization.



(**a**) (**b**)

Figure 9. SEM images of calcium phosphate powder: (**a**) crystalline; (**b**) amorphous.

The energy-dispersive spectroscopy (EDS) analysis of the powder is shown in Figure 10. The results indicate that the synthesized powder mainly consisted of Ca, P, and O, confirming that the powder was calcium phosphate, with a Ca/P ratio of approximately 1.63. This Ca/P ratio is very close to the stoichiometric value reported for hydroxyapatite (around 1.67) and aligns with the literature values for bioactive ACP powders (e.g., [21,22]). A slightly lower Ca/P ratio, as observed here, is often associated with increased reactivity and improved bioresorbability, which are especially desirable characteristics when integrating ACP into composite systems for controlled degradation and enhanced osseointegration in bone repair applications.



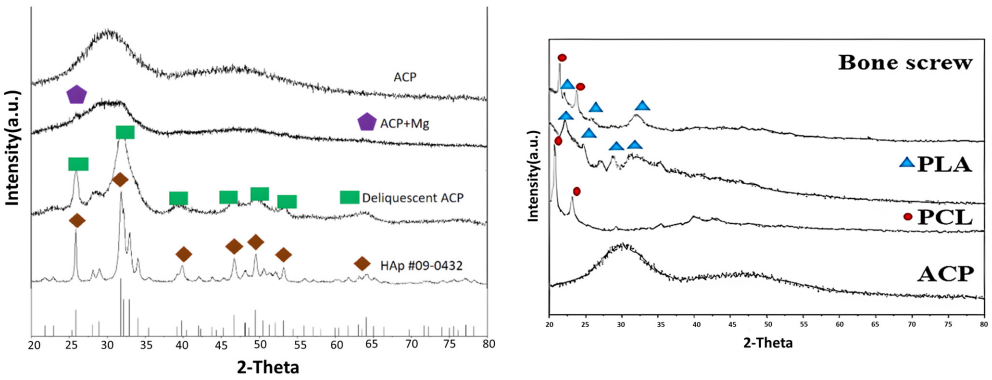
Element	Wt%	Wt%(Sigma)	Atomic(%)
O	50.54	1.10	69.90
Mg	0.67	0.29	0.61
P	15.75	0.84	11.25
Ca	33.04	0.89	18.24
Total:	100.00		100.00

Figure 10. EDS analysis of material composition.

3.1.2. X-Ray Diffraction Analysis

The synthesized material was confirmed to be a nanoscale calcium phosphate ceramic powder through SEM and EDS analyses. X-ray diffraction (XRD) was used to analyze the crystal structure of the calcium phosphate powder, and the results are shown in Figure 11a. The XRD pattern reveals that the as-synthesized ACP exhibits an amorphous structure, consistent with previous studies that report freshly prepared ACP lacks long-range crystallinity [22,31]. However, the improper storage of ACP after synthesis could lead to reactions with water vapor in the air, resulting in the deliquescence and crystallization of the synthesized powder. Indeed, our comparison with the reference diffraction pattern for commercial HAp (#09-0432) confirms that ACP crystallized into HAp after exposure to ambient conditions, as similarly documented in earlier studies [31]. To mitigate this phase transformation, we employed magnesium nitrate ($Mg(NO_3)_2 \cdot 6H_2O$) as a crystallization inhibitor. As reported in the literature [8], magnesium ions can react with PO_4^{3-} to form magnesium phosphate phases, effectively delaying the crystallization process. Additionally, vacuum packaging was used to prevent moisture-induced transformation, resulting in the successful preservation of the amorphous calcium phosphate ceramic powder.

Since the bone screw was primarily composed of PLA and PCL, XRD was performed on PLA, PCL, and the injection-molded bone screws. The results are shown in Figure 11b. The results confirmed that the bone screws were composed of PLA and PCL, and no calcium phosphate crystalline phases were detected. This indicates that the injection molding process did not trigger the crystallization of ACP, allowing the material to remain in its amorphous state—a desirable outcome supported by previous studies demonstrating that an amorphous state enhances bioactivity and ion release [22].



(**a**) (**b**)

Figure 11. XRD analysis: (**a**) calcium phosphate powder; (**b**) injection-molded bone.

3.2. Tensile Test

The compression-molded tensile specimens were subjected to tensile tests using a tensile testing machine to evaluate the tensile strength of the composites. Preliminary experiments showed that the addition of 30 wt.% ACP resulted in an excessively high powder content, which dramatically reduced the interfacial bonding between the polymer matrix and the ceramic particles, thereby compromising the moldability of the tensile specimens. Therefore, tests were conducted with ACP contents ranging from 5 to 20 wt.%. During testing, both ends of the specimen were clamped, and the specimen was stretched at a rate of 0.1 mm/s until it fractured. The data were recorded and analyzed, and the tensile test results are shown in Figure 12.

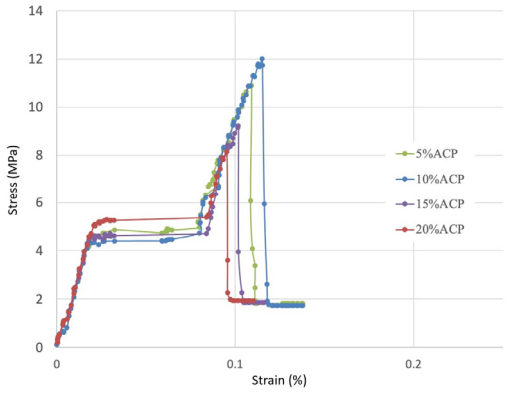


Figure 12. Results of tensile test.

Specimens with 10 wt.% ACP exhibited the best tensile strength, with a fracture strength of approximately 12 MPa. At strains of approximately 0.02–0.08%, a plateau in the stress–strain curve was observed, indicating a region where stress did not increase with further strain. This phenomenon may be attributed to stress relaxation and the optimal dispersion of the ceramic particles within the polymer matrix, which effectively enhances load transfer. Similar improvements in mechanical properties have been documented in previous studies, where an optimal ceramic powder content of 5–10% was found to enhance the tensile strength while excessive filler loading caused particle agglomeration and stress concentration [32]. Furthermore, Aliotta et al. [33] observed that the immiscibility between PLA and PCL often results in particle cavitation. In our study, the growth and aggregation of these cavitation zones along the tensile direction likely contribute to localized stress concentration and premature fracture, reaffirming the need for optimized filler content.

Overall, our results demonstrate that a 10 wt.% ACP content provides an optimal balance between reinforcement and matrix integrity, which is critical for maximizing

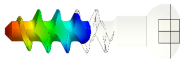
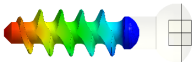
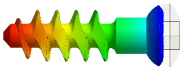
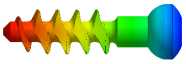
the tensile strength. This finding not only aligns with that of a previous study but also highlights the importance of fine-tuning composite formulations to mitigate issues such as particle agglomeration and cavitation in immiscible polymer systems.

3.3. Injection Molding

3.3.1. Short Shot Experiment

A short shot experiment was conducted by adjusting the metering settings of the injection molding machine to observe the flow behavior of the molten material filling the mold cavity. The short shot experiment results were compared with mold flow analysis, as shown in Table 4. The actual injection molding results were consistent with the mold flow analysis results.

Table 4. Results of short shot experiment.

Fill Rate	30%	50%	80%	100%
Actual				
Simulation				

3.3.2. Results of Taguchi Experiment

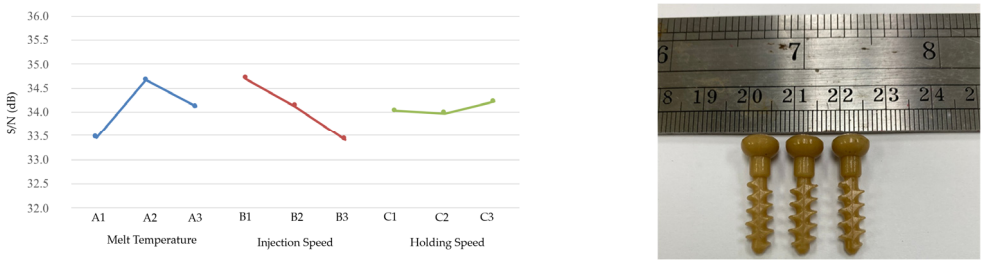
Five samples were molded for each parameter group in the Taguchi orthogonal array. The axial and radial dimensions of the bone screws were measured, and the shrinkage rates of the two dimensions were calculated. The average of the two values was used as the quality index to calculate the signal-to-noise (S/N) ratio, with the results presented in Table 5. Variance analysis results, shown in Table 6, revealed that the injection speed had the most significant impact on injection quality, contributing to 50.73%, followed by material temperature at 44.68%. The corresponding response diagrams in Figure 13a indicate that the optimal injection molding parameters were a material temperature of 190 °C (A2), an injection speed of 50 mm/s (B1), and a holding speed of 30 mm/s (C3), representing the combination identified through the Taguchi experiment. Verification of the optimal Taguchi combination yielded a shrinkage sum of 1.013% and an S/N ratio of 39.889, as detailed in Table 5. The bone screws produced under these optimal molding parameters are displayed in Figure 13b.

Table 5. Shrinkage sums and S/N ratios from the Taguchi experiment.

Group	Shrinkage Sum (%)	S/N Ratio
L1	2.02	33.892
L2	2.13	33.432
L3	2.225	33.053
L4	1.717	35.305
L5	1.838	34.715
L6	1.998	33.986
L7	1.829	34.758
L8	1.946	34.218
L9	2.187	33.204
Optimal	1.013	39.889

Table 6. Variance analysis.

Variance Analysis	**S**	**f**	**V**	**S′**	**ϱ**
Factor	Variation	Degree of Freedom	Variance	Pure Variation	Contribution
A	2.199	2.000	1.099	2.187	44.689
B	2.494	2.000	1.247	2.483	50.733
C	0.100	2.000	0.050	0.089	1.821
e(Error)	0.101	18.000	0.006	0.135	2.758
T(Total)	4.895	24.000		4.895	100.000

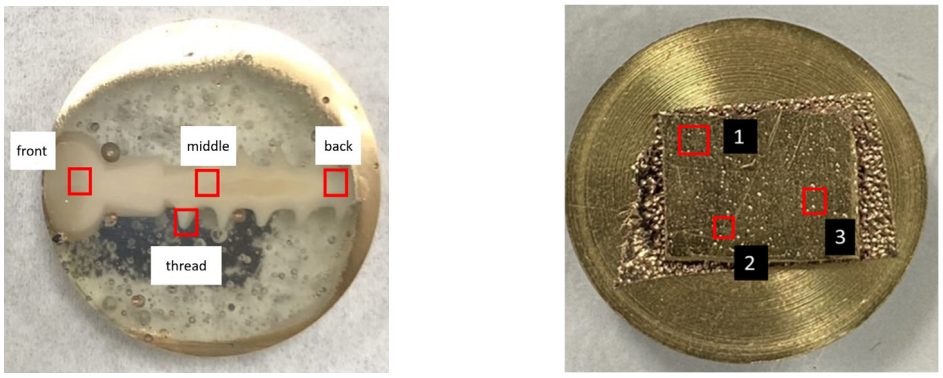


(**a**) (**b**)

Figure 13. (**a**) Response diagrams for control parameters; (**b**) bone screws molded under optimal parameters.

3.3.3. Screw Cross-Sectional Observation

The bone screw and PLA/PCL/ACP mixture were analyzed with EDS. The location of the bone screw analysis is shown in Figure 14, including the front, middle, back, and thread of the bone screw. The analysis results are shown in Tables 7 and 8, respectively. Examination of the SEM images revealed distinct white and black regions. The EDS analysis indicated that the white areas exhibited an average calcium content exceeding 9%, while the black areas contained less than 4% calcium. This contrast confirms that the white regions are rich in the calcium phosphate powder, whereas the black regions retain only trace amounts of the ceramic phase.



(**a**) (**b**)

Figure 14. Cross-sectional locations: (**a**) bone screws; (**b**) PLA/PCL/ACP composite.

Table 7. EDS analysis of bone screws.

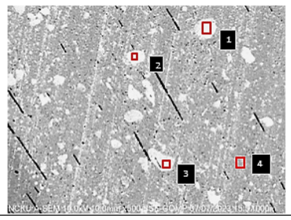
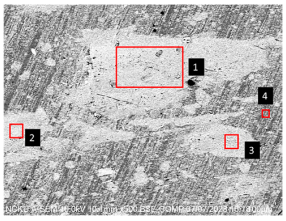
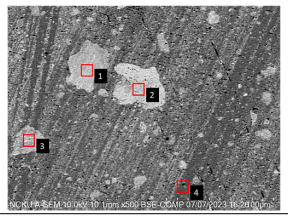
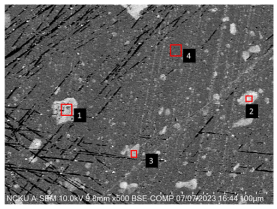
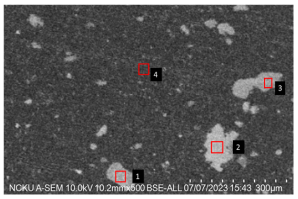
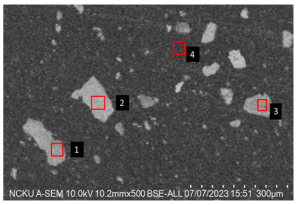
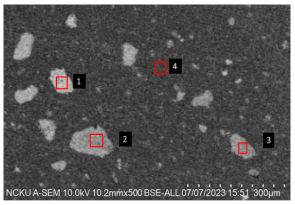
Location	SEM Image	EDS Position	Region	P (%)	Ca (%)	Average Ca (%)
Thread		1	White	11.8	12.4	9.9
		2		9.4	8.7	
		3		9.4	8.7	
		4	Black	8.7	3.2	3.2
Front		1	White	12.6	18.9	16
		2		11.9	15.5	
		3		12.3	13.6	
		4	Black	8.2	1	1
Middle		1	White	13.2	17.7	15.7
		2		12	14.3	
		3		12.4	15.1	
		4	Black	8.1	3.3	3.3
Back		1	White	12.5	14.3	13.2
		2		11.7	11.8	
		3		11.6	13.6	
		4	Black	8.9	3.9	3.9

Table 8. EDS analysis of composite material.

Location	SEM Image	EDS Position	Region	P (%)	Ca (%)	Average Ca (%)
1		1	White	12.7	13.6	13.4
		2		11.9	12.3	
		3		12.0	14.3	
		6	Black	7.2	2.1	2.1
2		1	White	11.5	12.4	12.9
		2		12.2	13.4	
		3		12.5	12.7	
		4	Black	5.6	2.6	2.6
3		1	White	13.4	18.4	15.5
		2		10.5	13.2	
		3		12.3	15.1	
		4	Black	2.9	0.3	0.3

Based on the color difference analysis results, as shown in Tables 9 and 10, the proportion of calcium phosphate powder in the bone screws was 8.02%, and the proportion in the composite material was 8.66%. These values closely match the intended addition of 10 wt.% ACP powder, suggesting the efficient dispersion of the ceramic phase and minimal loss during processing. This outcome is consistent with the previous reports on PLA/PCL composites reinforced with ceramic powders [12], where similar mixing efficiencies and uniform distributions were achieved. The alignment of the measured ceramic content with the target composition reinforces the validity of our processing methodology and indicates that the composite maintains the required ACP levels critical for enhanced bioactivity and mechanical performance.

Table 9. Color difference analysis of bone screws.

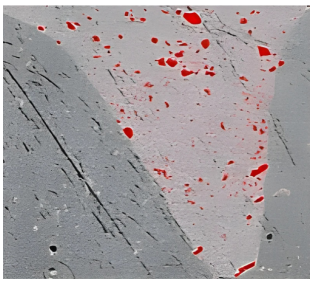
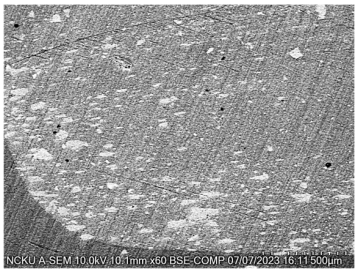
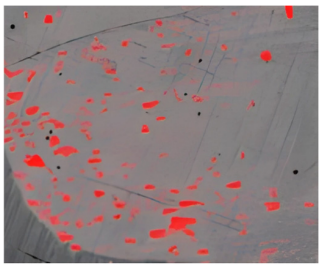
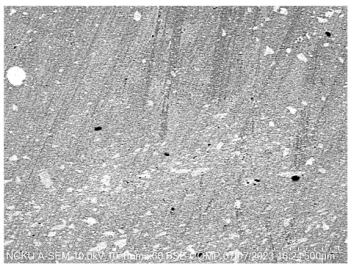
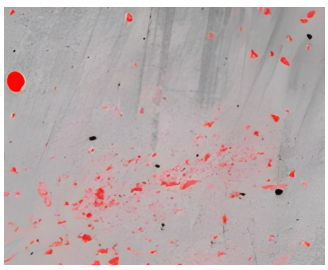
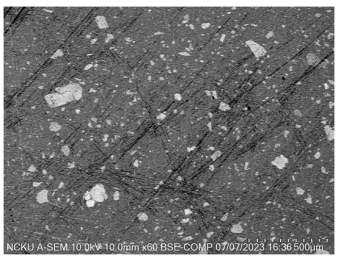
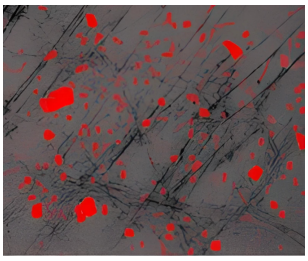
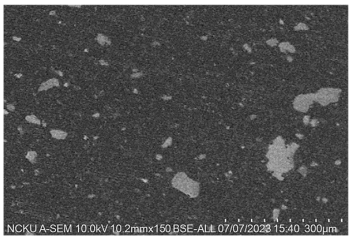
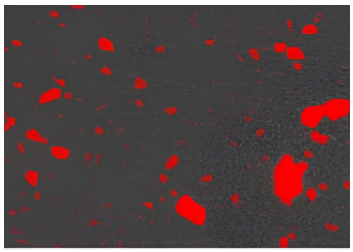
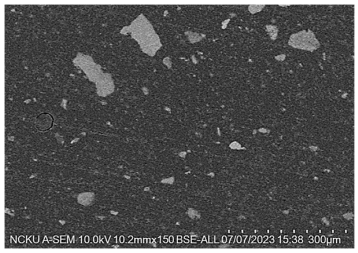
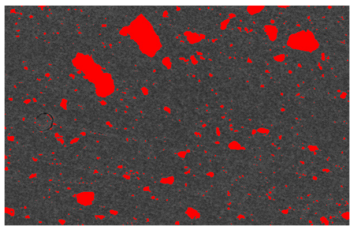
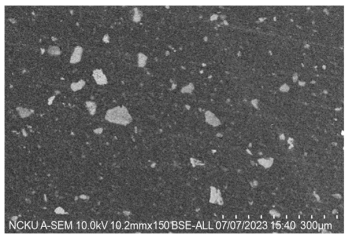
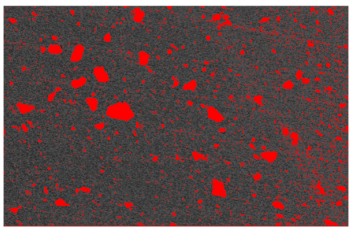
Location	Total Area (Pixel^2)	Red Area (Pixel^2)	%	SEM Image	Color Difference Map
Root	5.7	0.522	9.16%		
Front	16.658	1.26	7.56%		
Middle	17.812	1.236	6.94%		
Tail	17.5	1.471	8.41%		
	Average		8.02%	-	

Table 10. Color difference analysis of composite material.

Location	Total Area (Pixel^2)	Red Area (Pixel^2)	%	SEM Image	Color Difference Map
1	349,500	25,130	7.19%		
2	360,960	28,865	8.00%		
3	340,180	36,736	10.80%		
Average			8.66%	-	

3.3.4. Calcium Ion Dynamics in Simulated Body Fluid

This study measured the calcium ion concentration changes by immersing ACP and HAp in simulated body fluid (SBF) over time. The recorded data were plotted as concentration variation curves, shown in Figure 15. Through a blank titration, the calcium ion concentration in SBF was found to be approximately 350 ppm. After immersion, the initial calcium ion concentration of ACP and HAp decreased significantly, stabilizing after 5 h. After 6 h, the calcium concentration showed little change, with ACP reaching approximately 250 ppm, a decrease of 28%, and HAp reaching approximately 266 ppm, a decrease of 24%.

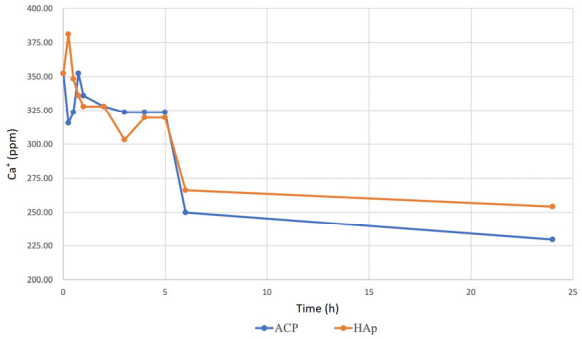


Figure 15. Calcium ion concentration variation curves.

According to a study by Kim et al. [34], HAp has an isoelectric point between 5 and 7 in water, while the pH of SBF is 7.4. This pH discrepancy facilitates the development of a negatively charged surface on HAp as phosphate and hydroxyl ions dissociate from

its crystal structure. Consequently, this negative surface attracts calcium ions from the SBF, leading to the formation of Ca-rich amorphous calcium phosphate (ACP). As the accumulation of Ca-rich ACP increases the positive surface charges, these charges interact further with the phosphate ions to form Ca-poor ACP, consuming additional calcium and phosphate ions. Moreover, the incorporation of trace magnesium and sodium ions promotes the eventual formation of bone-like apatite. These dynamic ion-exchange processes have been reported in the literature and are critical for understanding the apatite layer formation on bioactive materials.

These findings corroborate the previous study [34] and underscore the importance of controlled ion-exchange mechanisms in improving the bioactivity and osseointegration potential of implant materials.

3.4. Cell Test Results and Analysis

3.4.1. Biocompatibility Test (MTT Assay)

The biocompatibility of the PLA/PCL/ACP composites was evaluated using an MTT assay, and the results are shown in Figure 16. The data indicate that all three groups exhibited cell viability higher than 70%. According to the ISO 10993-5 standards, a cell viability above 70% is indicative of non-cytotoxic behavior, thereby confirming the good biocompatibility of the composites.

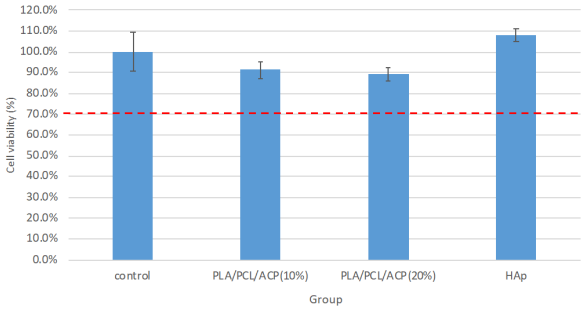


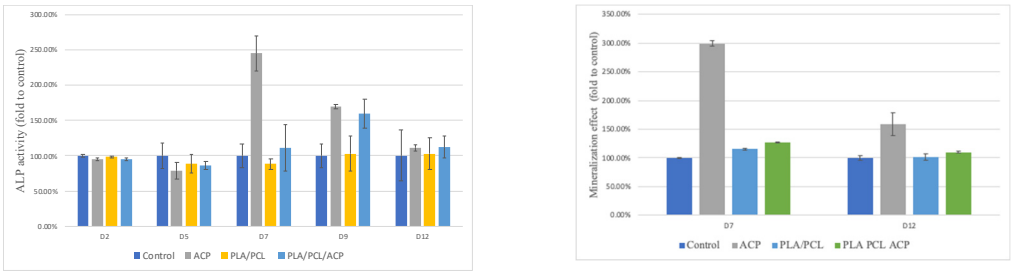
Figure 16. Biocompatibility test results.

Furthermore, the similar bioactivity observed in specimens containing 10 wt.% and 20 wt.% ACP suggests that the incorporation of ACP into the PLA/PCL matrix, within this loading range, does not adversely affect cell proliferation. Rather, it is likely that the presence of ACP contributes to a favorable surface chemistry and ion release profile that promote cell viability—findings that agree with those of a previous study [32] on ceramic-reinforced polymer composites.

3.4.2. Bone Differentiation and Mineralization Test

The results of the bone cell differentiation experiment from Day 2 (D2) to Day 12 (D12) are shown in Figure 17a. On D2 and Day 5 (D5), there was no significant difference in bone differentiation. Notably, by Day 7 (D7), the ACP group exhibited approximately 150% (±25%) higher bone differentiation than the control group, while the PLA/PCL/ACP composite showed about 20% (±7.5%) improvement over the PLA/PCL sample. These enhancements suggest that the incorporation of ACP accelerates early-stage differentiation.

On Day 9 (D9), the ACP group showed 70% (±2.9%) higher differentiation than the control group, but this gradually decreased over time. The PLA/PCL/ACP composite showed approximately 56% (±21%) higher differentiation than the PLA/PCL composite and 60% (±21%) higher differentiation than the control group.

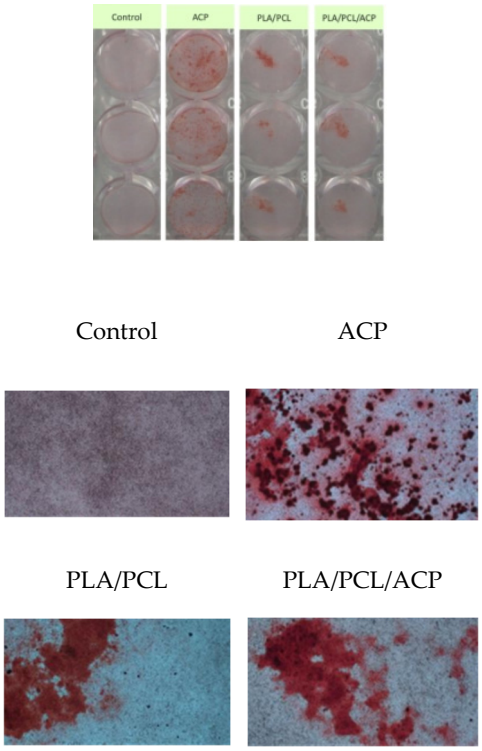


(**a**) (**b**)

Figure 17. (**a**) Bone cell differentiation results; (**b**) bone mineralization results.

According to a study by Choi et al. [35], bone cell differentiation can be divided into three stages: 1. the cell proliferation phase; 2. the bone matrix protein formation phase; and 3. the mineralization phase. In line with these stages, our data indicate that ACP exhibits a rapid enhancement in cell proliferation and differentiation by D7, implying an accelerated transition into the mineralization phase. Meanwhile, the PLA/PCL/ACP composite appears to modulate this process, reaching its mineralization peak by D9. This observation suggests that combining ACP with polymer matrices not only promotes early differentiation but also allows for controlled mineralization kinetics.

The results of the bone cell mineralization experiment on D7 and D12 are shown in Figures 17b and 18a,b. On D7, the ACP group exhibited approximately 200% (±5.2%) higher bone mineralization than the control group, and the PLA/PCL/ACP composite exhibited approximately 11% (±1%) higher bone differentiation and mineralization than the PLA/PCL composite. On D12, the ACP group still exhibited approximately 58% (±10%) higher mineralization than the control group, while the PLA/PCL/ACP composite exhibited approximately 8% (±1.8%) higher mineralization than the PLA/PCL composite.



(**a**)

Figure 18. *Cont.*

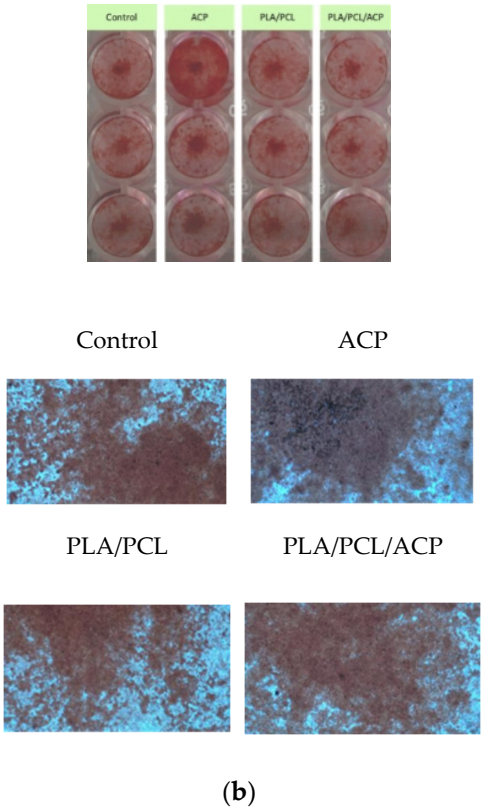


Figure 18. Mineralization analysis: (**a**) D7; (**b**) D12.

These findings clearly indicate that the addition of ACP significantly enhances both bone differentiation and the subsequent mineralization. In particular, while ACP alone drives rapid mineralization in the early phase, its incorporation into the PLA/PCL matrix results in a more controlled, sustained mineralization process. This controlled mineralization is critical for the long-term success of orthopedic implants, as it may better mimic the gradual bone formation observed in vivo. Such trends are consistent with previous studies, reinforcing the potential of ACP as a bioactive filler in composite systems [35].

3.5. Evaluation of Degradation Behavior

The degradation curve plotted from the weekly weight measurements of the bone screws is shown in Figure 19a. In the first week of the degradation test, the bone screw weight increased by an average of approximately 0.29%, which can be attributed to the rapid crystallization of ACP within the composite. This initial weight gain is consistent with the formation of a more stable crystalline phase, as described in a similar study [36]. Subsequently, the weight decreased continuously each week, with a reduction of about 2% by the fifth week, indicating that the overall degradation of the polymer matrix eventually outweighed the early-stage ACP crystallization effect.

The pH variation curve is shown in Figure 19b. Initially, the solution exhibited weak acidity due to ACP absorbing Ca^{2+} from the simulated body fluid (SBF) and undergoing crystallization. After 12 days, the pH dropped to 6.3, and then remained relatively stable, which contrasts with previous reports where the PLA/PCL composites without ACP exhibited pH values in the range of 3–4 after 16 days [36]. This suggests that the incorporation of ACP acts as a buffering agent, mitigating the acidification typically driven by polymer degradation.

After degradation, the bone screws were stained with Alizarin Red, as shown in Figure 20. Significant calcium deposition (red areas) was observed on the bone screws, which resulted from ACP crystallization causing calcium precipitation. These calcium-rich deposits not only confirm the occurrence of ACP crystallization during degradation but

may also indicate enhanced bioactivity that could promote bone regeneration. Based on the weekly degradation changes in the bone screws, as shown in Table 11, cracks appeared at the parting line of the bone screws after the fourth week, and degradation began from the cracks, suggesting that the formation of microcracks is a critical factor in accelerating the overall degradation process.

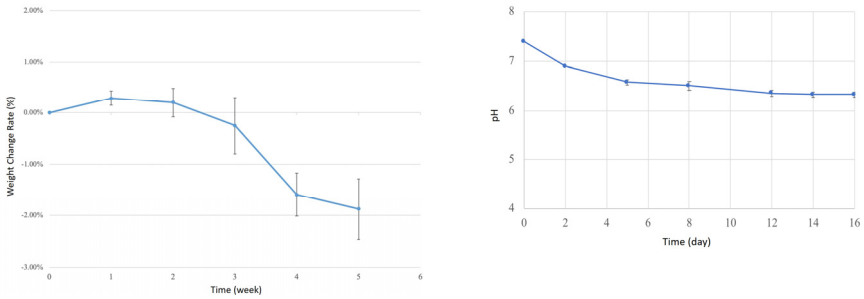


Figure 19. Analysis of degradation and pH variation: (**a**) degradation curve; (**b**) pH variation curve.



Figure 20. Calcium deposition on bone screws (rustic red areas).

Table 11. Illustrations of bone screw degradation.

Week	**0**	**1**
		
Week	**2**	**3**
		
Week	**4**	**5**
		

4. Conclusions

This study demonstrates the potential of biodegradable microinjection-molded PLA/PCL bone screws reinforced with amorphous calcium phosphate (ACP) for biomedical applications. The novel incorporation of nanoscale ACP significantly enhances the mechanical properties, biocompatibility, and bone differentiation/mineralization of the

composite—a distinctive approach that combines ceramic reinforcement with polymer matrices in a microscale injection molding process. Moreover, the optimization of molding parameters via the Taguchi experimental design ensures the consistent quality and improved performance of the bone screws.

The evaluation of degradation behavior, mechanical strength, and biocompatibility confirms that the bone screws are promising candidates for orthopedic use. Nevertheless, further insights into their long-term mechanical stability and degradation kinetics under cyclic, load-bearing conditions are needed to fully establish their clinical reliability.

Future research should focus on the following topics:

- Composite Optimization and Dynamic Testing: refining the composite formulation to further enhance mechanical strength and assessing its performance under cyclic, load-bearing conditions.
- In Vivo Validation: conducting in-depth animal studies and clinical trials to evaluate osseointegration, degradation behavior, and interface stability under physiological loads.
- Process Scalability: investigating the scalability of the optimized injection molding process to ensure feasibility for clinical production.

Overall, these findings underscore the critical role of material composition and process optimization in developing advanced biomaterials, while providing clear, actionable directions to bridge the gap between laboratory research and clinical application in this field.

Author Contributions: Conceptualization, M.-W.W., C.-C.T. and C.-M.C.; methodology, M.-W.W., W.-Y.W. and C.-M.C.; experiments, W.-Y.W.; software, W.-Y.W.; validation, M.-W.W.; formal analysis, M.-W.W. and W.-Y.W.; investigation, M.-W.W. and W.-Y.W.; writing—original draft preparation, M.-W.W. and W.-Y.W.; writing—review and editing, M.-W.W.; supervision, M.-W.W. and C.-C.T.; project administration, M.-W.W.; funding acquisition, M.-W.W. All authors have read and agreed to the published version of the manuscript.

Funding: This work was supported by the National Science and Technology Council, Taiwan, under grant number MOST 110-2221-E992-002.

Data Availability Statement: Data available within the article.

Acknowledgments: The authors acknowledge the use of AI tools, specifically Microsoft Copilot, during the preparation of the initial manuscript draft and the revision process. Copilot was employed to refine the language, enhance textual clarity, and ensure technical accuracy in descriptions. All experimental designs, data collection, analysis, and interpretations were performed solely by the authors without AI involvement.

Conflicts of Interest: The authors declare that they have no conflicts of interest.

References

1. Majewski, M.; Susanne, H.; Klaus, S. Epidemiology of athletic knee injuries: A 10-Year study. *Knee* **2006**, *13*, 184–188. [CrossRef] [PubMed]
2. Schatzker, J.; Meutstege, F.; Prieur, W.D. Implants and their application. In *Manual of Internal Fixation in Small Animals*, 2nd ed.; Brinker, W.O., Olmstead, M.L., Sumner-Smith, G., Prieur, W.D., Eds.; Springer: Berlin, Germany, 1998; pp. 57–96.
3. Junlei, L.; Ling, Q.; Ke, Y.; Zhijie, M.; Yongxuan, W.; Liangliang, C.; Dewei, Z. Materials evolution of bone plates for internal fixation of bone fractures: A review. *J. Mater. Sci. Technol.* **2020**, *36*, 190–208.
4. Merritt, K.; Brown, S.A. Metal sensitivity reactions to orthopedic implants. *Int. J. Dermatol.* **1981**, *20*, 89–94. [CrossRef] [PubMed]
5. Gefen, A. Optimizing the biomechanical compatibility of orthopedic screws for bone fracture fixation. *Med. Eng. Phys.* **2002**, *24*, 337–347. [CrossRef]
6. Wang, J.; Xu, J.; Liu, W.; Li, Y.; Qin, L. Biodegradable magnesium (Mg) implantation does not impose related metabolic disorders in rats with chronic renal failure. *Sci. Rep.* **2016**, *6*, 26341. [CrossRef]

7. Luo, L.; Zhang, C.; Wang, J.; Liu, F.; Chau, K.W.; Qin, L.; Wang, J. Clinical translation and challenges of biodegradable magnesium-based interference screws in ACL reconstruction. *Bioact. Mater.* **2021**, *6*, 3231–3243. [CrossRef]
8. Gu, X.N.; Xie, X.H.; Li, N.; Zheng, Y.F.; Qin, L. In vitro and in vivo studies on a Mg–Sr binary alloy system developed as a new kind of biodegradable metal. *Acta. Biomater.* **2012**, *8*, 2360–2374. [CrossRef]
9. Dhawan, A.; Ghodadra, N.; Karas, V.; Salata, M.J.; Cole, B.J. Complications of bioabsorbable suture anchors in the shoulder. *Am. J. Sports. Med.* **2011**, *40*, 424–1430. [CrossRef]
10. Webster, K.E.; Feller, J.A.; Kimp, A.J.; Whitehead, T.S. Revision anterior cruciate ligament reconstruction outcomes in younger patients: Medial meniscal pathology and high rates of return to sport are associated with third ACL injuries. *Am. J. Sports. Med.* **2018**, *46*, 1137–1142. [CrossRef]
11. Persson, A.; Gifstad, T.; Lind, M.; Engebretsen, L.; Fjeldsgaard, K.; Drogset, J.O.; Forssblad, M.; Espehaug, B.; Kjellsen, A.B.; Fevang, J.M. Graft fixation influences revision risk after ACL reconstruction with hamstring tendon autografts. *Acta. Orthop.* **2018**, *89*, 204–210. [CrossRef]
12. Hassanajili, S.; Karami-Pour, A.; Oryan, A.; Talaei-Khozani, T. Preparation and characterization of PLA/PCL/HA composite scaffolds using indirect 3D printing for bone tissue engineering. *Mater. Sci. Eng. C* **2019**, *104*, 109960. [CrossRef] [PubMed]
13. Wegst, U.G.K.; Bai, H.; Saiz, E.; Tomsia, A.P.; Ritchie, R.O. Bioinspired structural materials. *Nat. Mater.* **2015**, *14*, 23–36. [CrossRef] [PubMed]
14. Murugan, R.; Ramakrishna, S. Development of nanocomposites for bone grafting. *Compos. Sci. Technol.* **2005**, *65*, 2385–2406. [CrossRef]
15. Balasundaram, G.; Sato, M.; Webster, T.J. Using hydroxyapatite nanoparticles and decreased crystallinity to promote osteoblast adhesion similar to functionalizing with RGD. *Biomaterials* **2006**, *27*, 2798–2805. [CrossRef]
16. Smith, A.; Johnson, B.; Lee, C. Advances in injection molding: Process, materials and applications. *J. Manuf. Mater. Process.* **2021**, *5*, 34–56.
17. Iafisco, M.; Esposti, L.D.; Ramírez-Rodríguez, G.B.; Carella, F.; Gómez-Morales, J.; Ionescu, A.C.; Brambilla, E.; Tampieri, A.; Delgado-López, J.M. Fluoride-doped amorphous calcium phosphate nanoparticles as a promising biomimetic material for dental remineralization. *Sci. Rep.* **2018**, *8*, 17016. [CrossRef]
18. Falzarano, M.; Polettini, A.; Pomi, R.; Rossi, A.; Zonfa, T.; Bracciale, M.P.; Gabrielli, S.; Sarasini, F.; Tirillò, J. Anaerobic biodegradation of polylactic acid-based items: A specific focus on disposable tableware products. *Materials* **2022**, *15*, 6332. [CrossRef]
19. Feng, S.; Sun, L. Microstructure-based magneto-mechanical modeling of magnetorheological elastomer composites: A comparable analysis of dipole and Maxwell methods. *Materials* **2021**, *14*, 4251. [CrossRef]
20. Berger, J.; Mocciaro, A.; Córdoba, G.; Martinefsky, C.; Irassar, E.F.; Beuntner, N.; Scherb, S.; Thienel, K.C.; Tironi, A. Challenges and performance of filter dusts as a supplementary cementitious material. *Materials* **2020**, *13*, 5613. [CrossRef]
21. Martins, A.; Duarte, A.R.; Faria, S.; Marques, A.P.; Reis, R.L.; Neves, N.M. Osteogenic induction of hBMSCs by electrospun scaffolds with dexamethasone release functionality. *Biomaterials* **2010**, *31*, 5875–5885. [CrossRef]
22. Somrani, S.; Banu, M.; Jemal, M.; Rey, C. Physico-chemical and thermochemical studies of the hydrolytic conversion of amorphous tricalcium phosphate into apatite. *J. Solid State Chem.* **2005**, *178*, 1337–1348. [CrossRef]
23. Kiani, P.; Sedighi, M.; Kasaeian-Naeini, M.; Jabbari, A.H. High cycle fatigue behavior and thermal properties of PLA/PCL blends produced by fused deposition modeling. *J. Polym. Res.* **2023**, *30*, 264. [CrossRef]
24. Staffa, L.H.; Huysecom, A.-S.; Bettini, S.H.P.; Moldenaers, P.; Chinelatto, M.A. Effect of molecular structure of PEG/PCL multiblock copolymers on the morphology and interfacial properties of PLA/PCL blends. *J. Polym. Res.* **2022**, *29*, 388. [CrossRef]
25. *ASTM-D638-14*; The Definitive Guide to Plastic Tensile Testing. American Society for Testing and Materials: West Conshohocken, PA, USA, 2017.
26. TotalEnergies Corbion. Processing Guide: Injection Molding of Standard and High Heat PLA Compounds. 2022. Available online: https://www.totalenergies-corbion.com/media/ny1kwp02/processing-guide-injection-molding-of-standard-and-high-heat-pla-compounds-20220722.pdf (accessed on 2 February 2023).
27. Cheng, T.; Huang, Y.; Liang, Q. Effects of mold cooling channel design on temperature uniformity and warpage in injection molding. *J. Manuf. Process.* **2017**, *30*, 376–382.
28. International Organization for Standardization. *ISO 10993-5:2009—Biological Evaluation of Medical Devices—Part 5: Tests for In Vitro Cytotoxicity*; ISO: Geneva, Switzerland, 2009.
29. *ASTM-F1635-11*; In Vitro Degradation Testing of Hydrolytically Degradable Polymer Resins and Fabricated Forms for Surgical Implants. American Society for Testing and Materials: West Conshohocken, PA, USA, 2020.
30. Oyane, A.; Kim, H.M.; Furuya, T.; Kokubo, T.; Miyazaki, T.; Nakamura, T. Preparation and assessment of revised simulated body fluids. J. Biomed. *Mater. Res. A* **2003**, *65A*, 188–195. [CrossRef]

31. Chatzipanagis, K.; Iafisco, M.; Roncal-Herrero, T.; Bilton, M.; Tampieri, A.; Kröger, R.; Delgado-López, J.M. Crystallization of citrate-stabilized amorphous calcium phosphate to nanocrystalline apatite: A surface-mediated transformation. *Cryst. Eng. Comm.* **2016**, *18*, 3170–3178. [CrossRef]
32. Li, J.; Lu, X.L.; Zheng, Y.F. Effect of surface modified hydroxyapatite on the tensile property improvement of HA/PLA composite. *Appl. Surf. Sci.* **2008**, *255*, 494–497. [CrossRef]
33. Aliotta, L.; Gigante, V.; Geerinck, R.; Coltelli, M.B.; Lazzeri, A. Micromechanical analysis and fracture mechanics of poly(lactic acid) (PLA)/polycaprolactone (PCL) binary blends. *Polym. Test.* **2023**, *121*, 107984. [CrossRef]
34. Kim, H.M.; Himeno, T.; Kokubo, T.; Nakamura, T. Process and kinetics of bonelike apatite formation on sintered hydroxyapatite in a simulated body fluid. *Biomaterials* **2005**, *26*, 4366–4373. [CrossRef]
35. Choi, J.Y.; Lee, B.H.; Song, K.B.; Park, R.W.; Kim, I.S.; Sohn, K.Y.; Jo, J.S.; Ryoo, H.M. Expression patterns of bone-related proteins during osteoblastic differentiation in MC3T3-E1 cells. *J. Cell. Biochem.* **1996**, *61*, 609–618. [CrossRef]
36. Ahmadzadeh, Y.; Babaei, A.; Goudarzi, A. Assessment of localization and degradation of ZnO nanoparticles in the PLA/PCL biocompatible blend through a comprehensive rheological characterization. *Polym. Degrad. Stab.* **2018**, *158*, 136–147. [CrossRef]

Disclaimer/Publisher's Note: The statements, opinions and data contained in all publications are solely those of the individual author(s) and contributor(s) and not of MDPI and/or the editor(s). MDPI and/or the editor(s) disclaim responsibility for any injury to people or property resulting from any ideas, methods, instructions or products referred to in the content.